Research in Astron. Astrophys. **2009** Vol. **9** No. **8**, 933 – 944
http://www.raa-journal.org *http://www.iop.org/journals/raa*

Research in Astronomy and Astrophysics

Magnetic non-potentiality on the quiet Sun and the filigree *

Meng Zhao, Jing-Xiu Wang, Chun-Lan Jin and Gui-Ping Zhou

Key Laboratory of Solar Activity, National Astronomical Observatories, Chinese Academy of Sciences, Beijing 100012, China; *zhaomeng@bao.ac.cn*

Received 2009 January 20; accepted 2009 March 13

Abstract From the observed vector magnetic fields by the Solar Optical Telescope/Spectro-Polarimeter aboard the satellite *Hinode*, we have examined whether or not the quiet Sun magnetic fields are non-potential, and how the G-band filigrees and Ca II network bright points (NBPs) are associated with the magnetic non-potentiality. A sizable quiet region in the disk center is selected for this study. The new findings by the study are as follows. (1) The magnetic fields of the quiet region are obviously non-potential. The region-average shear angle is 40°, the average vertical current is $0.016\,\mathrm{A\ m^{-2}}$, and the average free magnetic energy density, $2.7\times10^{2}\,\mathrm{erg\ cm^{-3}}$. The magnitude of these non-potential quantities is comparable to that in solar active regions. (2) There are overall correlations among current helicity, free magnetic energy and longitudinal fields. The magnetic non-potentiality is mostly concentrated in the close vicinity of network elements which have stronger longitudinal fields. (3) The filigrees and NBPs are magnetically characterized by strong longitudinal fields, large electric helicity, and high free energy density. Because the selected region is away from any enhanced network, these new results can generally be applied to the quiet Sun. The findings imply that stronger network elements play a role in high magnetic non-potentiality in heating the solar atmosphere and in conducting the solar wind.

Key words: Sun: magnetic fields — Sun: photosphere — Sun: network bright point

1 INTRODUCTION

The term “magnetic non-potentiality” was first adopted by Wang et al. (1996) in a study of flare magnetism. Magnetic non-potentiality is a measure of the deviation of the observed vector magnetic fields from the potential configuration of current-free fields. The magnetic non-potentiality has been expressed by electric currents (Moreton & Severny 1968), shear angle (Hagyard et al. 1984; Lü et al. 1993), free energy density (Wang et al. 1996), and current helicity (Wang 1996; Abramenko et al. 1996), see a review by Wang (1999). A common consensus is that the energy that powers solar activity is stored in the stressed, non-potential magnetic fields. Therefore, the magnetic non-potentiality of solar active regions (ARs) serves as a measure of the productivity of solar activity.

While lots of studies have been carried out for ARs, to our knowledge, the only approach which addressed non-potential fields for the quiet Sun was made by Woodard & Chae (1999). Unfortunately, at that time, the vector field measurements for the quiet region were not available. Woodard and Chae use the fibril structure in Hα images as a proxy for the horizontal chromospheric magnetic field which

* Supported by the National Natural Science Foundation of China.

was compared with the horizontal field obtained by potential extrapolation of the observed, line-of-sight photospheric field. They concluded that quiet-Sun fields were "consistently and significantly non-potential in each of the three fields of view studied." They also found a relationship between magnetic reconnection and the magnetic non-potentiality in small-scale activity events, e.g., EUV blinkers.

For magnetic fields in ARs, it is commonly believed that the magnetic non-potentiality is either input from the solar interior during the emergence of pre-twisted flux ropes, or generated by the interaction of magnetic and velocity fields in the surface layer. Assume the magnetic field in the solar atmosphere is force-free, so it can be modeled by a force-free field, i.e.,

$$\nabla \times \boldsymbol{B} = \alpha(\boldsymbol{x}, t)\boldsymbol{B}. \tag{1}$$

The development of magnetic non-potentiality can thusly be described by the differential (or integral) equation of $\alpha(\boldsymbol{x}, t)$ (see Wang 1994), e.g.,

$$\frac{d\alpha}{dt} = \frac{1}{B^2}\nabla \cdot \{[(\boldsymbol{B} \cdot \triangledown)\boldsymbol{V} - (\boldsymbol{V} \cdot \triangledown)\boldsymbol{B}] \times \boldsymbol{B}\} + \boldsymbol{V} \cdot \triangledown\alpha. \tag{2}$$

In the derivation of this equation, the plasma has been assumed to be incompressible. The two terms on the right side of the equation represent, respectively, the generation mode and emergence mode of magnetic non-potentiality. The former comes from the interaction of the magnetic and velocity fields, i.e., the induction effect in which the gradients of both magnetic and velocity fields are central ingredients of the shear generation; while the latter is due to the transportation of non-potentiality, for instance, emergence of magnetic non-potentiality from the sub-surface layer.

In a similar way, Pevtsov et al. (1995) introduce a term of *twist* which is defined as

$$\alpha(\text{twist}) = \left\langle \frac{\boldsymbol{J}}{\boldsymbol{B}} \right\rangle = \left\langle \frac{1}{B_z}\left(\frac{\partial B_y}{\partial x} - \frac{\partial B_x}{\partial y}\right)\right\rangle. \tag{3}$$

Longcope et al. (1998) further propose that this twist is imparted to the flux through its interaction with turbulent velocities in the convection zone. This process, designated the $\sum$-effect, operates on isolated magnetic flux tubes that are subjected to buffeting by turbulence with a nonvanishing kinetic helicity $\langle \boldsymbol{u} \cdot \triangledown \times \boldsymbol{u}\rangle$. Su et al. (2008) consider the fact that in the deeper zone under the photosphere, the magnetic force may be less than the nonmagnetic force of plasma; while in the shallower zone, the magnetic force may be greater than the nonmagnetic force. Therefore, the vortical flow located beneath the photosphere would twist the flux tube and build up the magnetic non-potentiality in the tube; however, in the shallower layer, the stored magnetic free energy is released to drive the plasma to rotate in two opposite directions, e.g., in the depth ranges of 0 – 3(5) and 9 – 12 Mm, via Lorentz force. These authors also propose the concept of having a vector of non-potential magnetic stress.

The same physical processes would certainly happen on the quiet Sun. Moreover, the quiet Sun's magnetic fields appear weaker than those in ARs and smaller in spatial scale, and possibly shallower in anchoring. By the vigorous advection with the convection and localized flow in the convection zone, as well as in the photospheric layer, it should be expected that the magnetic fields on the quiet Sun are non-potential in nature.

Thanks to the great success of the Solar Optical Telescope/Spectro-Polarimeter (SOT/SP) aboard *Hinode* (Tsuneta et al. 2008; Suematsu et al. 2008; Ichimoto et al. 2008; Shimizu et al. 2008; Kosugi et al. 2007; Tarbell et al. 2007), for the first time, vector magnetic fields of the very quiet Sun have been measured with very high spatial resolution and adequate sensitivity (e.g., Centeno et al. 2007; Lites et al. 2007, 2008; Orozco Suárez et al. 2007a,b; Ishikawa et al. 2008; Jin et al. 2009). The advance in spatial resolution and sensitivity of SOT/SP observations afforded by *Hinode* provides us an opportunity to explore whether or not the quiet Sun magnetic fields are non-potential, and if the activity on the quiet Sun is associated with high magnetic non-potentiality, like that revealed for ARs. With this motivation, we select a very quiet region in the disk center. The region's field of view is big enough, e.g., 150×160 square arcsec, and the magnetic observations have good temporal coverage of G-band and Ca II filtergram observations for comparison.

The next section is a description of the observations. In Section 3, we present quantitative results on magnetic non-potentiality. Section 4 is devoted to the correlation of the magnetic non-potentiality with filigrees and NBPs. In the last section, we draw concluding remarks.

2 OBSERVATIONS

The Spectro-Polarimeter (SP) observations by the SOT instruments aboard the *H*inode spacecraft cover the wavelength range from 630.08 nm to 630.32 nm, providing the full Stokes spectral signals of two magnetically sensitive Fe I lines at 630.15 nm ($g_{\rm eff} = 1.67$) and 630.25 nm ($g_{\rm eff} = 2.5$). The spatial resolution of the SP observations is $0.32''$, and the wavelength sampling is 21.6 mÅ.

A quiet solar region with a field-of-view (FOV) of $151.14'' \times 162.30''$ was observed at the disk center on 2007 December 21 by using the SP. The data consist of 1024 consecutive positions of the spectrograph slit. For the observation of each spectrograph slit, the exposure time is 4.8 s, yielding a noise level of about $1.55{\times}10^{-3}$ Ic in Stokes Q and U, and $9.2{\times}10^{-4}$ Ic in Stokes V. The scanning steps of the spectrograph slit are $0.1476''$.

Vector magnetic fields are derived from the inversion of the full Stokes profiles based on the assumption of the Milne-Eddington (ME) atmospheric model. Inversion techniques are robust when applied to the stronger Stokes polarization signals, e.g., from solar ARs, but these profile-fitting procedures, which use many free parameters, typically encounter difficulties in convergence and uniqueness of the solutions when confronted with rather noisy profiles (Lites et al. 2008). Orozco Suárez et al. (2007a) suggest that ME inversion turns out to be largely independent of the noise and field strength initialization, provided they are applied to the pixels with polarization signals above a reasonable threshold. Accordingly, we only analyze those pixels with total polarization degree above approximately two times the noise level in the polarization continuum, which occupy approximately half of the total pixels. By this analysis, we exclude most of those profiles which cannot be inverted properly. We then apply a ‘median’ function to the inverted magnetogram to remove the unreliable noisy spikes.

The inversion returns the values of 13 free parameters, including the three components of magnetic fields (the field strength B, the inclination angle γ with respect to the line-of-sight (LOS) direction, the azimuth angle ϕ), the stray light fraction α, the Doppler velocity $V_{\rm Los}$, and so on. Martínez González et al. (2006) demonstrate that the pair of Fe I lines in the quiet Sun regions with low flux are not capable of distinguishing between the intrinsic magnetic field and the filling factor. Thusly, the apparent flux density (Lites et al. 1999) is a more appropriate quantity to describe the equivalent, spatially resolved vector magnetic fields, that is, the longitudinal component $B^L_{\rm app} = (1-\alpha)B\cos(\gamma)$ and the transverse component $B^T_{\rm app} = (1-\alpha)^{1/2}B\sin(\gamma)$. The $B^L_{\rm app}$ may be thought of as the magnitude of the LOS component that produces the observed circular polarization signal, while $B^T_{\rm app}$ is vertical to the LOS that would produce the observed linear polarization signal. The noise level is 4.8 Mx cm^{-2} (or G) for the LOS field, and 41.5 Mx cm^{-2} (G) for the transverse field. As this quiet region is centralized in the disk center, the LOS field stands for the vertical fields (VFs) and the transverse fields, for the horizontal fields (HFs) referring to the solar surface.

The Broadband Filter Imager (BFI) of SOT instruments provides G-band 4305 Å and Ca II H 3968 Å images, which cover most parts of the quiet region in the FOV of SP observations, with a cadence of 3 minutes from 00:22 to 01:49 on 2007 December 21. The FOV of these images is $223'' \times 112''$. The filtergrams are binned to $2{\times}2$ pixels in this observation, and the size of a binned pixel is $0.109''$.

The bright features of Ca II H and G-band images are grossly interpreted as the manifestations of small-scale magnetic flux concentrations (e.g., Spruit 1977; Sánchez Almeida et al. 2004). Thusly, we use the bright features to co-align these spectral images with the LOS magnetogram from SP observations. Spatially, we adopt the common FOV of SP and FG maps to make the co-alignment. Temporally, due to a longer acquisition time of the SP magnetic map, the SP map is cut into time-slices, each of which covers an interval of approximately 2 min. Then, we choose the corresponding slices in the G-band and Ca II images of the same temporal intervals to compose the synoptic spectral maps to compare with the magnetograms. The finally co-aligned SP magnetograms, synoptic G-band and Ca II filtergrams have a FOV of $1024{\times}696$ pixels with pixel size of $0.16''$ in each dimension.

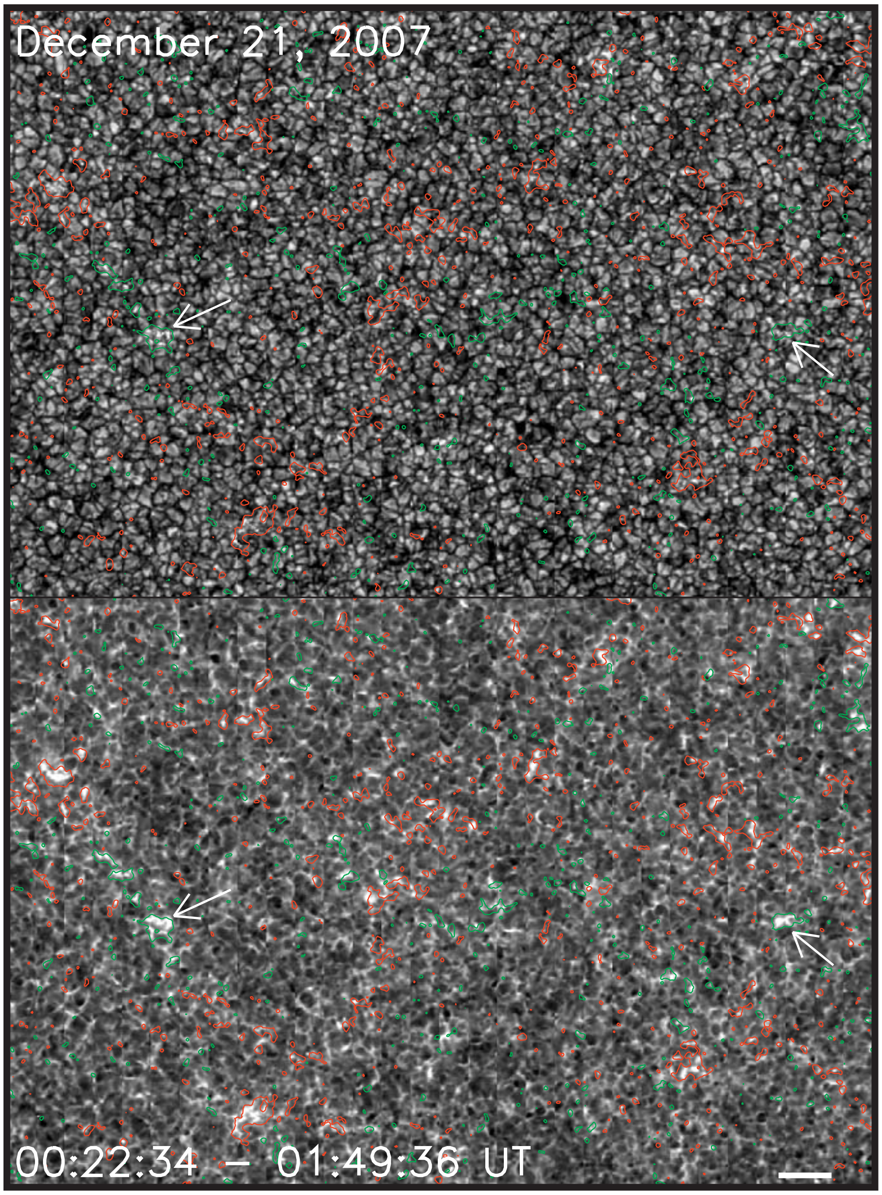

Fig. 1 Synoptic spectral images of G-band (*upper panel*) and Ca II H line (*lower panel*). Superposed on the images are contours of ± 50 G in the LOS magnetogram. Green (red) contours represent positive (negative) polarity. Two arrows indicate the G-band filigrees and Ca II NBPs. The bright bar in the lower-right corner denotes a scale of 10 arcsec in this and the following figures.

The synoptic spectral images for the G-band and Ca II H line are shown in Figure 1 with the contour of flux density of VFs superimposed. Generally speaking, the co-alignments between magnetograms and spectral images are satisfactory both in the temporal and spatial domains. However, the coincidence in time between magnetic and spectral images is only approximate with errors less than 2 min.

3 MAGNETIC NON-POTENTIALITY

3.1 Statistical Properties of Non-potential Parameters

A morphological comparison of the observed vector magnetic fields with the corresponding potential magnetic fields, which share the same longitudinal component with the observed vector fields, is shown in Figure 2. A few arrows highlight the places where there are clear non-potential characteristics of the observed horizontal fields (HFs). The magnetic non-potentiality is manifested in three aspects. First, the orientation (or equivalently, the azimuth) of the observed HFs deviates from that of the potential ones in many places (as indicated by Arrows 1, 2, and 4). Secondly, the field strength in term of the apparent flux density of HFs are different from the potential ones (as marked by Arrows 3 and 4). Thirdly, the observed horizontal fields are widely spread in weak VF places; while the potential ones are concentrated in the surroundings of the magnetic network of strong VFs (as indicated by Arrow 3). Lites et al. (2008) have commented about the apparent separation of the HFs from the VFs in quiet Sun observations.

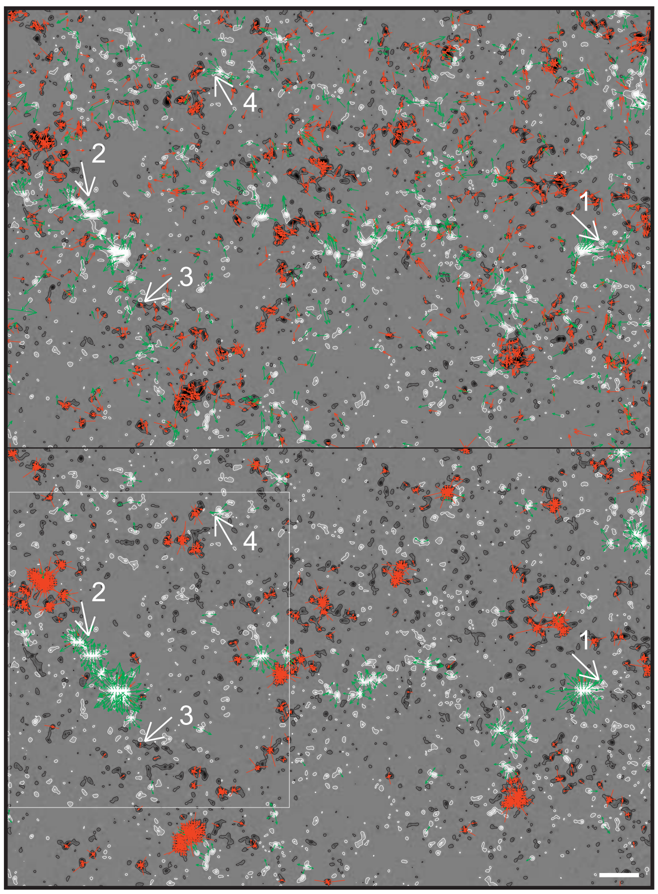

Fig. 2 Comparison of observed and potential vector magnetic fields. The contours are ± 20 and 100 G. Green (red) arrows represent HFs from positive (negative) polarity in VFs. In the magnetograms, the four arrows highlight the places where the observed vector fields obviously deviate from the potential fields. A frame in the figure shows a window for illustration.

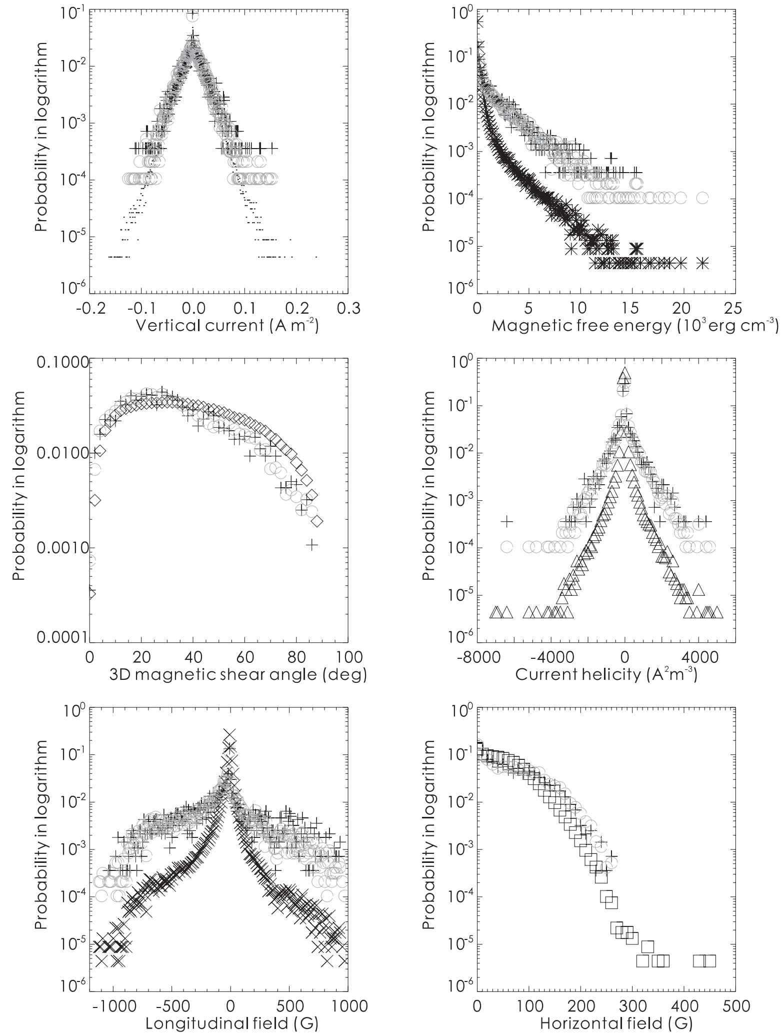

Fig. 3 PDFs of non-potential magnetic parameters. The plus and circle symbols in each panel represent the PDF for *G*-band filigrees and Ca II NBPs for later description. The other symbols in each panel show the PDFs of vertical current, free magnetic energy, shear angle, current helicity, VF and HF, respectively.

Quantitative measurements of the magnetic non-potentiality in term of vertical current, shear angle, current helicity, and free magnetic energy density have been made for each pixel with polarization signals above two times the sensitivity. The probability distribution function (PDF) of each non-potential parameter is shown in Figure 3. The PDFs of HFs and VFs are also shown in the same figure with the purpose of getting a general idea about the statistical properties of the quiet region which we studied. The statistical averages of the non-potential parameters are listed in Table 1. The 3D shear angle (Lü et al. 1993) has a broad distribution in the quiet region with the peak at approximately 30–40 degrees and an average of 40 degrees. The vertical current and current helicity are generally balanced in sign and the signed average is almost exactly zero. The same is true for the VF flux density. The VF, free energy density and current helicity have clear excessive tails in the PDF distribution. The detailed statistics of the magnetic non-potential parameters are shown in Table 1. Again, the VF and HF statistical properties are listed for reference.

Table 1 PDFs of Magnetic Non-potential Parameters

Parameters	Mean	Deviation	Maximum
Vertical Field (G)	35.2	78.5	1117.8
Horizontal Field (G)	56.5	42.5	457.0
Vertical Current (A m^{-2})	0.016	0.016	0.239
Shear Angle (degree)	40.6	20.2	90.0
Free Energy Density (10^2 erg cm^{-3})	2.67	6.96	218.2
Current Helicity (A^2 m^{-3})	54.1	165.3	6999.6

Taking the vertical current in the photosphere as a representative nonpotential parameter, the average current of the quiet region is 0.016 A m^{-2} and the maximum current, 0.24 A m^{-2}, is comparable with that in a normal solar AR. For a sizable AR, AR 6233, Wang et al. (1996) calculated the average current of 0.01–0.02 A m^{-2}, and de La Beaujardiere et al. (1993) and Wang et al. (1996) found a maximum current of 0.2 A m^{-2}.

3.2 Overall Correlations among the Non-potential Parameters

The distribution of magnetic parameters and their overall correlations in the quiet Sun are very diffuse (see Jin et al. 2009). This reflects the turbulent nature of the quiet Sun's magnetism.

To understand the mutual relationship between the turbulent magnetic parameters, a procedure named "*sort-group*" (SG), is suggested. Of course, only the measurements at the pixels with high-enough polarization signals can be chosen for the analysis. First, we sort all the parameters according to the strongness of the observed unsigned flux density of VFs as the later is a primary parameter in quantifying many aspects of the physics, such as the magnetic dichotomy, the magnetic convection, the flux tube property and so on. Secondly, for the sorted data, we group each of the 1,000 pixels into a data point, and assign their average value of magnetic parameters to each data point. For our case, 226 groups are formed, i.e., each data series has 226 data points. Thirdly, the new data sequences of magnetic parameters are correlated with one another.

It is worth noticing that in each group, a parameter often has a large deviation around its statistical mean. A scatter plot of grouped VFs and HFs in Figure 4 illustrates the turbulent nature of the distribution. For each value of the VF, the HF has a broad range of scatter. However, by the sort-group correlation (SGC), the statistical correlation between VFs and HFs in the quiet region is revealed in a clear way. The trend of the correlation is interesting. Starting from the weak VF to the flux density of 100 G, the HF increases with VF. In the range from 100 – 150 G of VF, the HF reaches the peak of the distribution at the magnitude of approximately 90 G. Afterwards, the HF decreases with an increase of VF, and finally when the VF is stronger than 400 G, the HF stays at the level of 60 G. This trend of correlation may represent the typical behavior of the quiet Sun's magnetic fields. The VF can be as strong as over 1 kG, while the HF would never be stronger than 1 kG. However, the average HF is stronger than that of VF.

The SGC emphasizes the global statistical properties. The overall correlations between various pairs of parameters are listed in Table 2, and a few scatter plots of SGC are shown in Figure 5. As illustrated, the scatters of non-potential parameters are rather big, and we have not plotted the deviation of each parameter on the figure.

The magnetic free energy on the photosphere has a very close correlation with VF and current helicity. The correlation coefficient is over 0.96. The Ca II brightness is highly correlated with VF, free energy, and current helicity. These correlations seem to imply that the magnetic elements with strong VFs are the dominant resource of magnetic free energy on the quiet Sun, like strong sunspots in ARs, and contribute greatly to the heating of the atmosphere. It is of interests to notice that the 3D shear angle maintains negative correlations with all the other parameters. Statistically, shear angles are larger

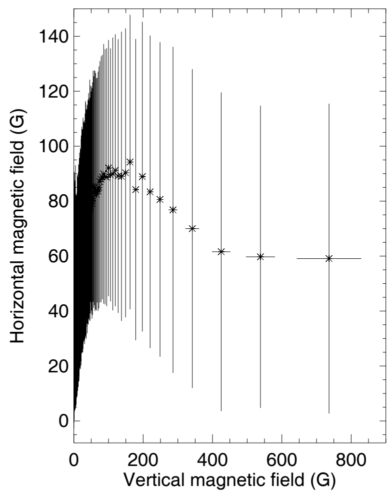

Fig. 4 Scatter plot of sorted and grouped VFs and HFs with error bars.

Table 2 SGCs of Magnetic Parameters

B_z	B_t	Cur	Shr	Hel	Erg	I_{gb}	I_{ca}
B_z	0.43	0.44	–0.86	0.98	0.96	0.81	0.95
B_t		0.97	–0.62	0.51	0.44	–0.02	0.63
Cur			–0.67	0.54	0.47	–0.03	0.66
Shr				–0.90	–0.94	–0.55	–0.94
Hel					0.98	0.77	0.97
Erg						0.77	0.93
I_{gb}							0.64

in weak VF elements in the quiet Sun, which are similar to those in ARs. Shear angle alone does not appear to be a good indicator of potential activity on the quiet Sun.

For the first time, we have determined the magnetic non-potentiality on the quiet Sun. It would be of great importance to diagnose whether or not the activity on the quiet Sun is intrinsically associated with the non-potential nature of the magnetic fields. We make a particular examination of the association between filigrees and Ca II bright points and the derived magnetic non-potentiality.

4 MAGNETIC NATURE OF FILIGREES AND CA II BRIGHT POINTS

Filigrees are a pattern of strings of small bright points which are visible in the photosphere. They were first observed in the wings of Hα lines by Dunn & Zirker (1973). The bright points forming the filigree are very clearly seen in G-band images. Ca II bright points were first detected by Mehltretter (1974) and found to be identical with the filigrees and with the photospheric faculae as seen near the limb. Observations at the disk center (Wilson 1981) further demonstrated that faculae, filigrees and Ca II bright points are different manifestations of the same phenomena. Very recent observations of Ca II bright point and filigrees were reported by Pérez-Suárez et al. (2008), de Wijn et al. (2008), and Bovelet & Wiehr (2008).

Filigrees and Ca II bright points are representative of active events on the quiet Sun and are transient in brightness. Therefore, we identify the filigrees and Ca II bright points from scrutinizing the G-band and Ca II movie made from Hinode observations. In the observed FOV, clear events of 119 filigrees and

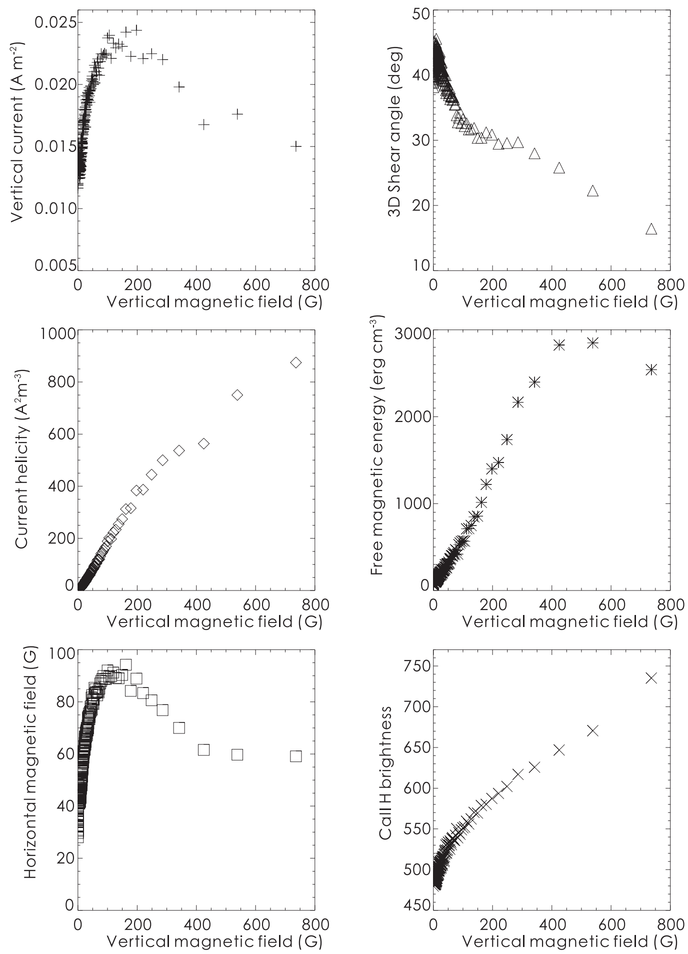

Fig. 5 SGCs of magnetic parameters.

Table 3 Statistics of Non-potential Parameters in the Filigree (Ca II Bright Point)

Parameters	Mean	Deviation	Maximum
Vertical Field (G)	221.5 (205.6)	236.4 (229.6)	1031.9 (1117.8)
Horizontal field (G)	61.1 (66.6)	53.5 (54.9)	268.5 (268.5)
Vertical Current (A m^{-2})	0.017 (0.017)	0.010 (0.017)	0.154 (0.154)
Shear Angle (degrees)	38.8 (38.1)	23.7 (23.0)	90.0 (90.0)
Free Energy density (10^2 erg cm^{-3})	15.70 (15.54)	21.56 (21.51)	154.00 (218.80)
Current Helicity (A^2m^{-3})	309.2 (293.3)	498.1 (487.0)	6732.0 (6732.0)

107 Ca II bright points are identified (see Fig. 1). They are closely related but do not exactly coincide spatially.

The statistical magnetic properties of the filigree and Ca II bright point are listed in Table 3 in the same way as Table 1. In the table, the mean properties of Ca II bright point are in the brackets. The PDFs of magnetic parameters in the filigree and Ca II bright point are superimposed on Figure 3 by symbols of pluses and circles in a slightly lighter color. It is very obvious that the filigree and Ca II bright point

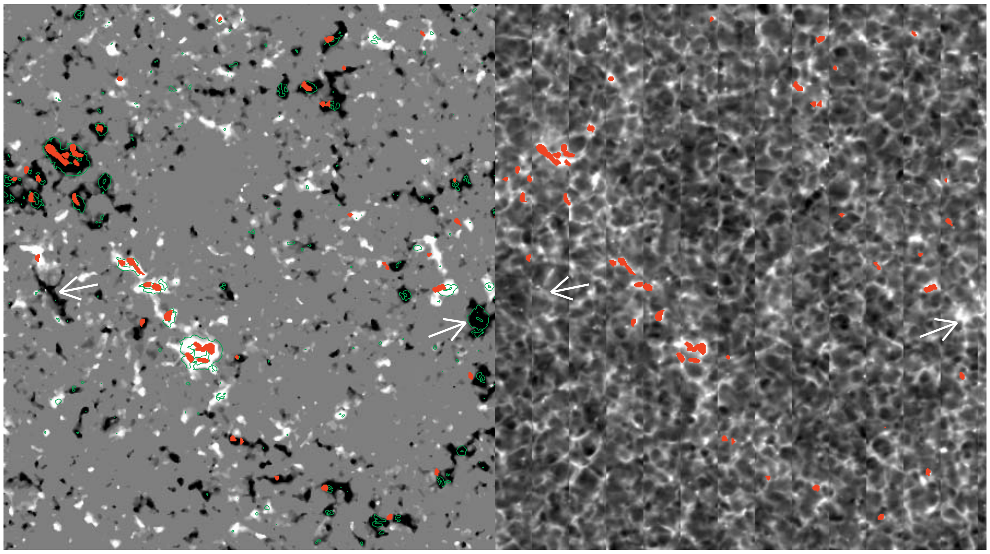

Fig. 6 *Left*: filigrees superimposed on the LOS magnetogram as red nuts; *Right*: filigrees superimposed on the Ca II image. Green contours represent the high free energy areas with free energy density higher than 1.0×10^3 erg cm^{-3}. The left arrow indicates a stronger VF patch with lower free energy density and no association to the filigree and Ca II point; the right arrow indicates a strong network element with high free energy and with association to the Ca II bright point but without a filigree.

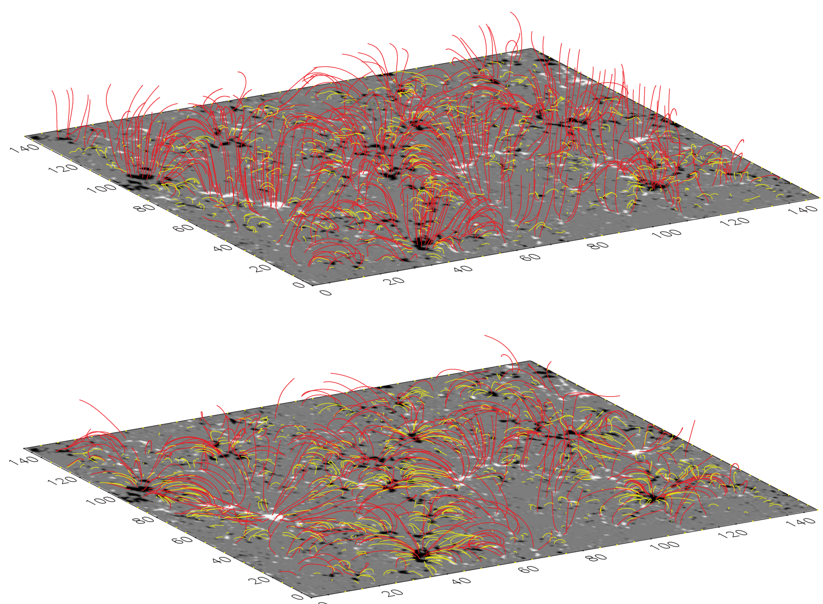

Fig. 7 *Top*: Force-free field reconstruction based on the observed vector magnetograms; *Low*: Potential field reconstruction based on the observed LOS magnetogram.

have a common magnetic nature. They are characterized by strong VF, high current helicity and large magnetic free energy. Their mean VF, current helicity, and free energy density are 4–6 times larger than those of the whole quiet region.

To especially illustrate their magnetic nature, we draw an enlarged frame for a typical network region (roughly a supergranule cell) in Figure 6 (see the frame outlined in Fig. 2).

Generally speaking, the filigrees and Ca II bright points are co-spatial, though not exactly identical in shape and location. They mostly appear within the strong VF elements which have high free energy density. In the figure, the left arrow indicates a strong VF flux patch which has low free magnetic energy density. Interestingly, the stronger magnetic elements are not associated with either a filigree or Ca II bright point. Sometimes, a flux patch has an association with a Ca II point but no relation to a filigree. An arrow on the right shows an example of this case.

5 CONCLUSIONS AND DISCUSSION

1. The magnetic field of the studied solar quiet region is clearly non-potential. The magnitude of non-potential magnetic parameters, e.g., the vertical currents and free magnetic energy density, is comparable with that in ARs. As the region is a typical solar quiet region and deviates from the enhanced magnetic network, the revealed magnetic non-potentiality would be representative of the quiet Sun.
2. Filigrees and Ca II bright points are magnetically characterized by a strong vertical magnetic field, high current helicity and high free magnetic energy density. The VF, current helicity, and free energy are 4–6 times stronger than those of the normal quiet Sun. This seems to imply that the magnetic non-potentiality of the quiet Sun is playing a similar active role in the quiet Sun activity as that in ARs. The high correlation of Ca II brightness with magnetic non-potentiality and strong VF suggests that the strong magnetic VF elements with high magnetic non-potentiality are more responsible for atmospheric heating.

We tentatively reconstruct the 3D magnetic field structure for the observed quiet region by using the quasi-linear force free code (Wang et al. 2001) and the boundary condition from the observed vector magnetograms. The results are shown in Figure 7 in comparison with a potential extrapolation with the boundary condition from the observed LOS magnetogram. By drawing the same numbers of magnetic lines of force, it is found that the force-free field reconstructed from the observed vector field on the photosphere extends much higher than the corresponding potential field. The reconstruction with the boundary condition from a non-potential vector field on the photosphere may correctly represent the 3D magnetic structure which is favored for explaining solar wind acceleration and coronal heating, since more magnetic lines of force extend to the height above the transition region (4–5 Mm) with current flowing.

This study presents the first results of the quiet Sun's magnetic non-potentiality based on vector magnetic field measurements, facilitated by SOT/Hinode. The SOT/SP data selected for this study are normal mode observations with exposure times of 4.8 s. The sensitivities of the derived vector magnetograms are not high enough. We take the threshold of 2σ polarization sensitivity for SP inversion, so that about half of the pixels in the observed FOV were lost in the derived magnetograms. This may result in two problems. First, on the weak field end, we simply lose the information about magnetic non-potentiality. The determined magnetic non-potentiality could be biased toward to the strong VF. Secondly, we may not be able to make a good reconstruction of the 3D magnetic structure in the corona because of the incomplete measurements of vector fields on the photosphere.

As this is the first approach that uses the magnetic non-potentiality on the quiet Sun, we do not attempt to make a detailed comparison of magnetic non-potentiality on the quiet Sun and in ARs. A vector magnetic field on the quiet Sun measured with a large FOV and based on deep mode SOT/SP observations would be desired. Meanwhile, the SOT/SP observations should have good temporal coverage of G-band and Ca II observations. That data would be of great help for a more thorough quantitative diagnosis of the magnetic non-potentiality on the quiet Sun. With that database, we may also make a further examination of various resolutions of the 180 degree ambiguity in determining the field azimuth. More efforts on the origin of coronal heating and solar wind acceleration need to be made based on the vector magnetic field observations on the quiet Sun.

Acknowledgements The authors are grateful to the *Hinode* team for providing the data. *Hinode* is a Japanese mission developed and launched by ISAS/JAXA, with NAOJ as a domestic partner and NASA and STFC (UK) as international partners. It is operated by these agencies in cooperation with ESA and NSC (Norway). This work is supported by the National Natural Science Foundation of China (10873020, 10703007, G10573025, 40674081, 10603008, 10733020 and 40890161), the Chinese Academy of Sciences Project KJCX2-YW-T04, and the National Basic Research Program of China (G2006CB806303).

References

Abramenko, V. I., Wang, T. J., & Yurchishin, V. B. 1996, Sol. Phys., 168, 75
Bovelet, B., & Wiehr, E. 2008, A&A, 488, 1101
Centeno, R., Socas-Navarro, H., Lites, B., et al. 2007, ApJ, 666, L137
de La Beaujardiere, J. F., Canfield, Richard C., & Leka, K. D. 1993, ApJ, 411, 378
de Wijn, A. G., Lites, B. W., Berger, T. E., et al. 2008, ApJ, 684, 1469
Dunn, R. B., & Zirker, J. B. 1973, Sol. Phys., 33, 281
Hagyard, M. J., Teuber, D., West, E. A., & Smith, J. B. 1984, Sol. Phys., 91, 115
Ichimoto, K., Lites, B., Elmore, D., et al. 2008, Sol. Phys., 249, 233
Ishikawa, R., Tsuneta, S., Ichimoto, K., et al. 2008, A&A, 481, 25
Jin, C. L., Wang, J. X., & Zhao, M. 2009, ApJ, 690, 279
Kosugi, T., Matsuzaki, K., Sakao, T., et al. 2007, Sol. Phys., 243, 3
Longcope, D. W., Fisher, G. H., & Pevtsov, A. A. 1998, ApJ, 507, 417
Lites, B. W., Rutten, R. J., & Berger, T. E. 1999, ApJ, 517, 1013
Lites, B., Socas-Navarro, H., Kubo, M., et al. 2007, PASJ, 59, 571
Lites, B. W., Kubo, M., Socas-Navarro, H., et al. 2008, ApJ, 672, 1237
Lü, Y. P., Wang, J. X., & Wang, H. N. 1993, Sol. Phys., 148, 119
Mehltretter, J. P. 1974, Sol. Phys., 38, 43
Moreton, G. E., & Severny, A. B. 1968, Sol. Phys., 3, 282
Martínez González, M. J., Collados, M., & Ruiz Cobo, B. 2006, A&A, 456, 1159
Orozco Suárez, D., Bellot Rubio, L. R., Del Toro Iniesta, J. C., et al. 2007b, PASJ, 59, 837
Orozco Suárez, D., Bellot Rubio, L. R., Del Toro Iniesta, J. C., et al. 2007a, ApJ, 670, L61
Pérez-Suárez, D., Maclean, R. C., Doyle, J. G., & Madjarska, M. S. 2008, A&A, 492, 575
Pevtsov, A. A., Canfield, R. C., & Metcalf, T. R. 1995, ApJ, 440, L109
Sánchez Almeida, J., Márquez, I., Bonet, J. A., et al. 2004, ApJ, 609, L91
Shimizu, T., Nagata, S., Tsuneta, S., et al. 2008, Sol. Phys., 249, 221
Spruit, H. C. 1977, PhDT, 237
Su, J. T., Liu, Y., Liu, J. H., Mao, X. J., Zhang, H. Q., Li, H., Wang, X. F., & Xie, W. B. 2008, Sol. Phys., 252, 55
Suematsu, Y., Tsuneta, S., Ichimoto, K., et al. 2008, Sol. Phys., 249, 197
Tarbell, T. D., Lites, B. W., Shine, R. A., et al. 2007, AAS, 210, 9401
Tsuneta, S., Ichimoto, K., Katsukawa, Y., et al. 2008, Sol. Phys., 249, 167
Wang, H. N., Yan, Y. H., & Sakurai, T. 2001, Sol. Phys., 201, 323
Wang, J. X., Shi, Z. X., Wang, H. N., & Lü, Y. P. 1996, ApJ, 456, 861
Wang, J. X. 1994, Sol. Phys., 155, 285
Wang, J. X. 1996, Sol. Phys., 163, 319
Wang, J. X. 1999, FCPH, 20, 251
Wilson, P. R. 1981, Sol. Phys., 69, 9
Woodard, M. F., & Chae, J. C. 1999, Sol. Phys., 184, 239